energies

MDPI

Article

Rapid Estimation Technology of Fuel Cell Internal State Based on Single Frequency Impedance Phase Angle Measurement: A Case Study

Wei Nie [1,2], Kai Li [1,*], Wang Zhang [2], Renkang Wang [1] and Hao Tang [1,*]

[1] School of Automation Engineering, University of Electronic Science and Technology of China, Chengdu 611731, China; 202112060935@std.uestc.edu.cn (W.N.); renkangwww@uestc.edu.cn (R.W.)
[2] Wuhan Institute of Marine Electric Propulsion, Wuhan 430064, China; zhanggoodwang@163.com
* Correspondence: kaili@uestc.edu.cn (K.L.); tanghao@uestc.edu.cn (H.T.)

Abstract

Improper internal states in proton exchange membrane fuel cells (PEMFCs), such as insufficient reactant concentration, lower membrane water content, and excessive liquid water, will lead to significant reductions in durability and reliability, which is a bottleneck restricting the large-scale commercial application of the PEMFC system. Closed-loop management with internal state feedback is regarded as a promising strategy for prolonging its lifespan and enhancing its reliability. The key issue for the closed-loop management strategy is how to estimate the internal operating state of the PEMFC stack accurately and quickly. Consequently, an estimation method of stack internal operating states based on the medium frequency impedance phase angle measurement, which has the characteristics of short acquisition time, small measurement error, and high resolution, is proposed in this paper. The sensitivity, monotonicity, correlation analysis in the steady state, and response characteristics analysis in the dynamic state show that the proposed method is effective, competent, and qualified for internal state estimation. Then, the estimated internal state is applied to the system's closed-loop management as feedback. The experiment results show that the PEMFC can be maintained at the expected state and that improper states will be avoided. The proposed estimation technology will significantly facilitate the system's closed-loop management, thereby enhancing the reliability and durability of PEMFCs.

Keywords: proton exchange membrane fuel cell; fuel cell system; internal state estimation; electrochemical impedance spectroscopy; impedance phase angle; closed-loop management

Academic Editors: Julian Jepsen and Julian Puszkiel

Received: 22 December 2025
Revised: 6 February 2026
Accepted: 13 February 2026
Published: 17 February 2026

1. Introduction

As an important hydrogen energy utilization mode, the proton exchange membrane fuel cell (PEMFC) offers high energy conversion efficiency, high power density, fast room-temperature start-up, low noise, and zero pollution, which is expected to alleviate the energy crisis and reduce carbon dioxide emissions. It has broad application prospects in rail transit, aerospace, and other fields [1]. In transportation applications, the fuel cell (FC) often faces frequent power changes. In this dynamic situation, the FC system needs to regulate operating variables (gas flow, pressure, humidity, temperature) of the air supply, hydrogen supply, and thermal management auxiliary subsystem to create suitable electrochemical reaction conditions for the FC stack and obtain high-performance output for the FC system. If the conditions are regulated improperly, the FC may be in an improper operating state and even cause membrane drying, flooding, and other faults [2–5]. These faults and improper operation states of FC will significantly reduce the reliability and durability of the FC system, which is the bottleneck restricting its large-scale commercial application.

To facilitate system management for prolonging the service life and enhancing the reliability of the FC stack, internal state real-time estimation is imperative for feedback control to maintain the internal state at the expected levels [6]. Similar to the internal combustion engine's closed-loop control of fuel and oxidizer supply strategy based on internal combustion state estimation [7], the key issue of the internal state closed-loop control strategy for the FC system is how to accurately and quickly estimate the internal operating state (including fault) of the FC stack. Suppose the internal state can be accurately obtained in real time. In that case, the supply strategy of hydrogen and air, the pressure and temperature of the stack can be adjusted in a closed-loop management strategy according to the internal state feedback to make the FC stack work in a suitable state and avoid failure and improper operating conditions.

Many scholars have conducted much research on the FC internal state estimation. The existing literature can be classified as model-based, data-driven, and experiment-based methods [6,8–13].

The principle of the model-based estimation method is to evaluate the difference between the actual measured value and the model-calculated value [8,14]. The operating state is judged according to the different characteristics. This method features a short delay time and low computational cost, making it suitable for real-time evaluation. However, such methods require precise mastery of the fuel cell system's mechanisms and parameters. Fixed parameters are difficult to adapt to full operating conditions, necessitating additional optimization algorithms [15]. In addition, FC's multi-time scale and multi-parameter coupling characteristics will reduce model-based methods' observability and estimation accuracy, resulting in insufficient robustness.

The data-driven estimation method establishes an effective identification mechanism by analyzing, learning, and mining the state-related information underlying the historical operation data of the FC system. Many developed data-driven estimation algorithms [15–23] exist, such as neural networks, support vector machines, support vector data description, and spherical structure support vector machines. These methods can avoid system modeling and lack of prior expert knowledge, and feature strong pertinence and good expandability for the identification of key states and fault variables. The drawback is that its performance is highly dependent on the quality and quantity of training data. A trade-off must be made between computational cost and real-time performance.

Experiment-based estimation methods mainly include image visualization, printed-circuit board (PCB) sensing, and electrochemical impedance spectroscopy (EIS). Visualization technology uses neutron imaging [24], X-ray imaging [25], or magnetic resonance imaging [26] to directly observe the character of the stack's internal state (predominantly liquid water). This kind of method can intuitively explore the mechanism of stack internal states. The drawback is the requirements for costly and bulky instruments and equipment. Therefore, it is often used in laboratory development and cannot be used in application systems. PCB sensing technology [27,28] installs a PCB embedded with current, temperature, or humidity sensors into the FC stack and estimates the operating state by analyzing the distribution parameters measured by sensors. The drawback is that the measured parameter can only reflect the local information of the stack and lacks the overall characterization. In a broad sense, EIS [3,29] technology can be understood as a high-precision, broadband, and non-destructive sensor that is sensitive to both external operation factors (such as temperature, humidity, pressure, mass flow, and load current) and internal factors (such as material body, interface, composition, and fabrication process) of the FC stack [30]. From the perspective of system operation, EIS as a characterization tool can be used to determine the suitable working range of FC [31,32], diagnose and identify faults in the stack [5,33,34], assess the state of health of the aged PEMFC [35,36], etc.

The effectiveness of EIS technology has been verified in numerous studies. The full impedance spectrum contains rich state information, such as the electrochemical reaction and the water state inside the stack. However, the long measurement time of EIS leads to many limitations in practical applications. The complete spectrum measurement of electrochemical impedance is usually obtained by sweeping frequency, which generally takes several minutes. The time scale of minutes is quite long for real-time state estimation of dynamic and time-varying FC systems. To reduce the time required for wideband impedance measurement, researchers have proposed many advanced methods, such as hybrid multi-frequency disturbance [37,38], pseudorandom binary sequence [39,40], and maximum length sequence [41]. The measurement time of the full impedance spectrum can be significantly reduced to about 30 s. However, this time is still too long for fast, real-time estimation of the internal state of the FC aiming at closed-loop management.

Shortening the time of impedance acquisition and preserving the internal state-related information contained in EIS are key issues that need to be dealt with for its real-time application. The mass transfer impedance most affected by flooding can be described by the EIS's low-frequency (LF) impedance. The ohmic resistance, which is most affected by membrane drying, can be described by the high-frequency (HF) impedance. Based on the above consensus, the measured value of the imaginary part of impedance at 0.5 Hz and the measured value of the real part of impedance at 1 kHz were used to evaluate the water-containing state of FC [42]. However, FCs are dynamic operating systems, and the measured LF impedance fluctuates too much, making it easy to be disturbed by noise in practical applications [43]. Literature [44] analyzed the evolvement rule of the ohmic resistance of the proton exchange membrane during the process from drying to normal to flooding. The HF impedance intercept of the real axis represented the ohmic resistance of the membrane, and the intercept value was used as the basis for fault diagnosis. This method can effectively diagnose membrane drying faults, but cannot be used to evaluate the internal excess liquid water state.

To obtain a fast and real-time method to estimate the internal operating state of FC, this paper proposes a simple and effective method based on single-frequency impedance phase angle measurement. Firstly, the full impedance spectrum is tested for an FC stack under numerous steady-state conditions, and the performance characteristics of the impedance spectrum, amplitude-frequency characteristics, and phase-frequency characteristics of the stack are analyzed. Based on the analysis results, an FC internal state estimating method based on the impedance phase angle at medium frequency (MF) is proposed. The sensitivity, effectiveness, rapidity, and anti-interference ability are evaluated, and the impedance phase angle application value for closed-loop operation management is discussed. Secondly, the impedance phase angle dynamic response characteristics under the step change of two preferred operating variables, cathode air stoichiometric ratio and stack operating temperature, are studied and analyzed. Then, the relationship between the operating condition's input and the state's output (impedance phase angle) can be obtained to facilitate the design of a system's closed-loop management strategy. Finally, with the proposed internal operating state estimation as feedback, the cathode air supply and the stack operating temperature could be adjusted in real time by the closed-loop management strategy to ensure the PEMFC operates in a suitable state and avoids improper operating conditions.

2. Necessity of Internal State Estimation for Fuel Cell System Management

From the perspective of system integration and operation, the output voltage performance of FC is mainly affected by seven operating variables: cathode air pressure (kPa), cathode air stoichiometric ratio λ_{ca} (dimensionless), cathode air humidity RH_{ca} (%), anode hydrogen pressure (kPa), anode hydrogen stoichiometric ratio λ_{an} (dimensionless), anode hydrogen humidity RH_{an} (%), and stack operating temperature T_{stk} (°C). Since the micron thickness of the proton exchange membrane in the stack can only withstand a slight pressure difference, the pressure of the cathode air and the anode hydrogen should be kept equal during operation. Thus, these two operating variables, cathode air pressure and anode hydrogen pressure, have only one regulatory goal: the stack operating pressure P_{stk} (kPa). Consequently, λ_{ca}, RH_{ca}, λ_{an}, RH_{an}, P_{stk}, and T_{stk} are six adjustable operating variables for the FC stack. These six operating variables build the stack's operating environment, represented by the following vector: $\mathbf{X} = (\lambda_{ca}, RH_{ca}, \lambda_{an}, RH_{an}, P_{stk}, T_{stk})$. Therefore, the voltage performance of the stack V_{stk} (V) under the current density i_{stk} (A/cm^2) condition is the function of operating variables and can be expressed by Equation (1):

$$V_{stk} = f_{i\text{-}stk}\,(\lambda_{ca}, RH_{ca}, \lambda_{an}, RH_{an}, P_{stk}, T_{stk}) \quad (1)$$

To obtain the demand operating environment for FC, it is usually necessary to conduct several performance evaluation tests through the FC characteristic test platform and take the long-term stable operation of the voltage change rate $\Delta V_{stk}/t$ less than a pre-set value as the evaluation criterion. The fundamental demand operating variable vector $\mathbf{X^0} = (\lambda^0_{ca}, RH^0_{ca}, \lambda^0_{an}, RH^0_{an}, P^0_{stk}, T^0_{stk})$ under different i_{stk} conditions can be obtained. Then, an operating variable lookup table with i_{stk} as the index can be constructed, providing a fundamental operating environment for FC system management.

Figure 1a shows the conventional management strategy for the FC system. The fundamental operating variable vector $\mathbf{X^0}$ is obtained by looking up the table according to the demand i_{stk} of the stack and set as the reference condition $\mathbf{X^*} = \mathbf{X^0}$ for three auxiliary subsystems. The conventional management strategy focuses on regulating the auxiliary subsystems: air supply, hydrogen supply, and thermal management. Each subsystem pays attention to the achievement of its control task. For example, the air supply subsystem needs to adopt decoupling control of air mass flow and pressure to suppress the overshoot in the transition process and reduce the risk of damage to the Membrane Electrode Assembly (MEA) caused by pressure and flow fluctuations. A load current feedforward control is essential for the hydrogen supply subsystem to realize pressure stability control under dynamic conditions and avoid fuel starvation. Thermal management subsystems often adopt prediction control to prevent temperature fluctuations caused by their significant hysteresis characteristic. In summary, the purpose of closed-loop control in conventional management strategy is to quickly and precisely create fundamental operating variable $\mathbf{X^*}$ for the good operation of the FC stack. Although each auxiliary subsystem has internal closed-loop control, from the perspective of the whole system operation, the setting of each operating variable is derived from a pre-set lookup table, and the operating variable is not dynamically adjusted according to the FC state obtained in real-time. This operational mechanism means that the internal states of the FC are uncontrollable. Therefore, the essence of the conventional FC system management method is an open-loop method.

As we know, it is not easy to create stable, reliable, and fully decoupled operating conditions in FC application systems compared with the well-constructed test bench. The stack will enter an improper operating state because of the imprecise operating conditions and unpredictable disturbances. In summary, the open-loop management method cannot

https://doi.org/10.3390/en19041049

correct deviations, and the reliability and robustness of the FC system are weak. The open-loop operation management method cannot meet the requirements for a high-quality system operation. To this end, it is crucial to develop a proper technology to maintain the internal states at the expected levels and avoid unexpected faults and improper states.

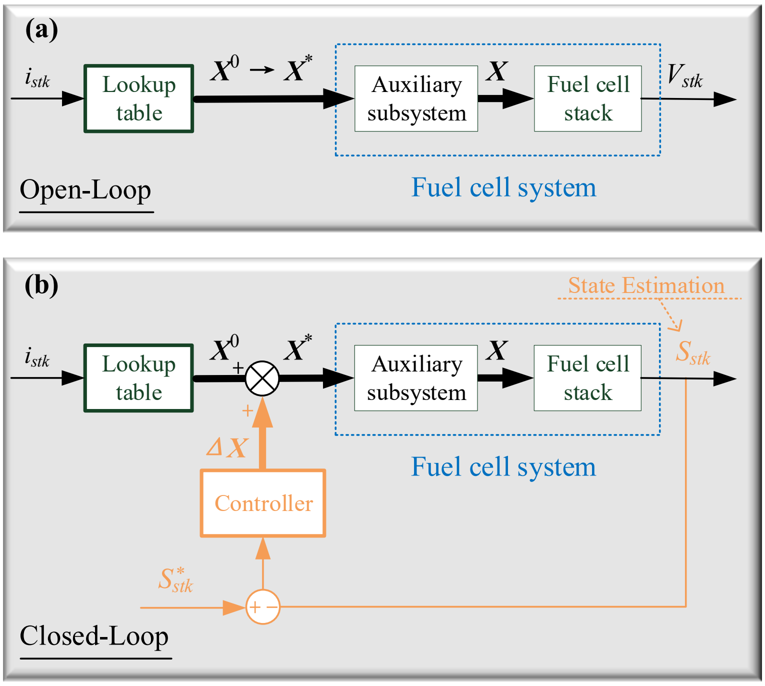

Figure 1. FC system management methods: (**a**) open-loop management without state feedback, (**b**) closed-loop management with state feedback.

A closed-loop management method with FC internal operating state feedback is proposed for improving the reliability and robustness of the FC system, as shown in Figure 1b. Comparing the conventional open-loop management strategy, the basic principle of closed-loop management strategy is as follows: the operating condition vector **X*** is dynamically adjusted according to the FC stack internal state S_{stk} feedback. Furthermore, the adjustment amount **ΔX** is calculated by the closed-loop controller according to the difference between the feedback state S_{stk} and reference state S^*_{stk}. The superscript * in this paper indicates the reference or the target value. As seen from Figure 1 (bottom), there are three critical steps to build a closed-loop management system. The requirements and purpose of each step will be elaborated as follows:

(1) Estimation of the FC stack internal state

The key point to building a closed-loop control system is quickly and effectively estimating the S_{stk} of the FC stack and establishing an appropriate control target S^*_{stk}. It is expected that the measurement process should be fast, have low disturbance (little impact on the original system), and have high precision (the accuracy of the operating state measurement determines the precision of the closed-loop management). In this paper, the complete impedance spectrum characteristics under different operating environments **X** are comprehensively analyzed in Section 4. Then, a simplified impedance variable that meets the requirements of real time and accuracy for feedback parameters is obtained as S_{stk}. Since the closed-loop control target and the unit negative feedback variable have the same physical properties, the control target S^*_{stk} is also the simplified impedance information.

(2) Analysis of internal state in the dynamic condition (operating variable step change)

To facilitate closed-loop controller design, it is necessary to clarify the response characteristics S_{stk} of the FC system under dynamic operating conditions **ΔX**. (labelled as $\boldsymbol{\Delta X} \rightarrow S_{stk}$). The purpose of dynamic response testing is to quantify the response characteristic from operating conditions to the optimal impedance information (same as S_{stk}). In this paper, the dynamic response characteristics of the FC system are tested and analyzed under the step change of two preferred operating variables in Section 5. Through dynamic results analysis, the time scale characteristic and equivalent transfer function of the controlled object in the control loop can be obtained.

(3) Design of a closed-loop management strategy in application

The dynamic response test results will provide the basis for the controller parameters' design in applying a closed-loop management strategy. Based on this, the controller parameters, including the proportional parameter, integral parameter, and control period, are designed according to the dynamic response test results of the selected operating variable. The effectiveness of the closed-loop management strategy will be verified in Section 6.

3. Fuel Cell Stack Characteristic Test Bench for State Estimation

3.1. Introduction of the Fuel Cell Stack and Its Test Bench

In this paper, the water-cooled graphite plate stack developed for high-power commercial vehicle applications is taken as the object of study, and a short stack consisting of 12 cells in series is used for experimental testing. The effective reaction area of MEA is 330 cm^2, the thickness of the PEM is 15 μm, the platinum load of the cathode is 0.35 mg/cm^2, and the platinum load of the anode is 0.05 mg/cm^2. To accurately obtain the operation characteristics of the stack under different operating conditions, the FC test bench shown in Figure 2 is used in this paper. The test bench can provide an accurate and decoupled operating variable vector X required by the stack.

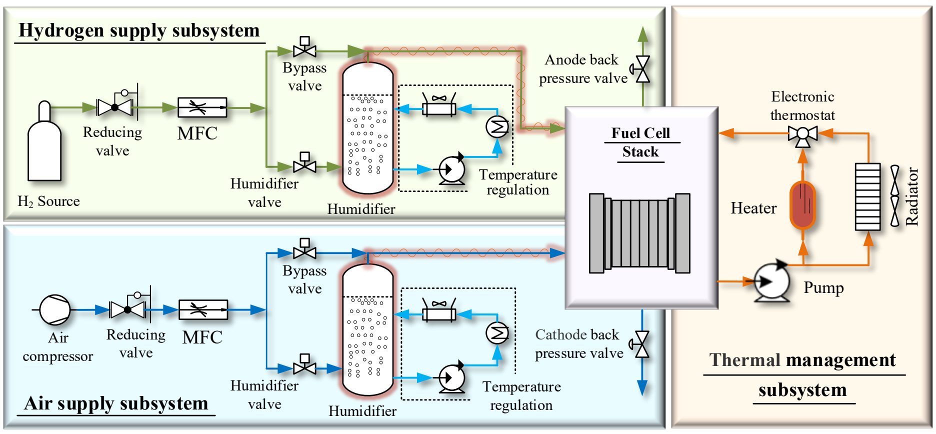

Figure 2. Fuel cell stack test bench.

As shown in Figure 2, the hydrogen comes from the high-pressure hydrogen cylinder, which is regulated to 0.5~1 MPa by a pressure-reducing valve. The λ_{an} for the stack is precisely controlled by a Mass Flow Controller (MFC), which is a Type 8741 product manufactured by Burkert (Germany). The humidifier used in this bench is a bubble and spray mixed humidifier and adopts a 100% saturation humidifier control mode. The temperature of the deionized water in the humidifier is approximately the dew point temperature of the gas at the output port. Thus, the relative humidity of the anode hydrogen can be calculated from the temperature and pressure of the stack. To avoid condensation of wet hydrogen due to heat conduction, the pipe between the humidifier and the stack is wrapped with a heating cable. The RH_{an} can be regulated by adjusting the water temperature in the humidifier. A parallel bypass branch of the humidifier is only used for fast switching and will be used for the humidity dynamic response test in Section 5.

After the reaction of input hydrogen in the stack, the remaining gas of the anode is directly drained through the back pressure valve. The anode hydrogen pressure is controlled by adjusting the opening of the anode back pressure valve.

The cathode air comes from the screw air compressor, and the compressed gas is stored in a 2 m^3 buffer tank after dusting and drying. The cathode air λ_{ca} regulation, RH_{ca} regulation, and cathode air pressure regulation are similar to those of anode hydrogen, which will not be described here. The P_{stk} is controlled by adjusting the opening of the anode and the cathode back pressure valve.

The operating temperature of the stack T_{stk} is maintained by regulating the pump, radiator fan, heater, and electronic thermostat in the thermal management subsystem. In this paper, T_{stk} is expressed by the temperature of the coolant entering the stack.

3.2. Online Impedance Measuring Scheme of FC Stack

The impedance measuring system of the FC stack is shown in Figure 3, which mainly consists of an electrochemical workstation and a programmable electronic load. The electrochemical workstation model is Metrohm PGSTAT304 (Metrohm, Switzerland). The built-in Frequency Response Analyzer (FRA) FRA32M is the core module for impedance measurement. The programmable electronic load model is Chroma 63206A (Chroma, Taiwan). As shown in Figure 3, the PGSTAT304 outputs the reference disturbance current signal I_{ref} to the electronic load, and the 63206A executes the current loading according to the reference disturbance current signal. In addition, the 63206A measures the actual current I_{mea} and feeds back to PGSTAT304. PGSTAT304 measures the disturbance current I_{mea} and the stack response voltage V_{mea}, and calculates the AC impedance. It is worth mentioning that the disturbance current is applied to the stack through the current-collecting plate to minimize contact resistance. The amplitude of the AC disturbance current used in this paper is 5% of the stack current i_{stk}.

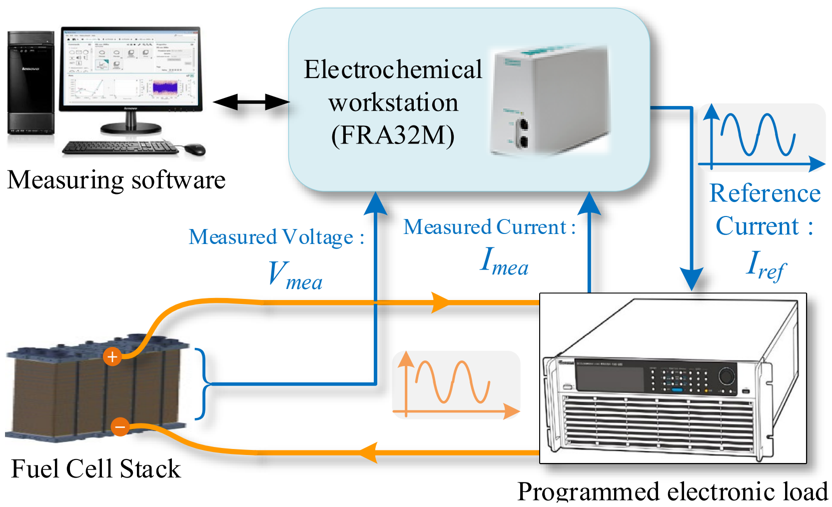

Figure 3. Online impedance measurement scheme.

4. Estimation of Stack Internal State Based on Impedance Characteristics Analysis in Steady-State

Based on the fundamental operating variable vector $\mathbf{X}^0$, one operating variable is changed to obtain the impedance spectrum's characteristics, and the operating variable's influence on the impedance spectrum is quantitatively analyzed. According to the results of steady-state response characteristics, the key information is extracted from the impedance spectrum, and the optimal impedance information suitable for the internal operating state S_{stk} feedback is determined.

4.1. Impedance Spectrum Testing Scheme of FC Stack

The fundamental demand operating variable vector $\mathbf{X^0} = (\lambda^0_{ca}, RH^0_{ca}, \lambda^0_{an}, RH^0_{an}, P^0_{stk}, T^0_{stk})$ of the tested FC stack under different i_{stk} conditions can be obtained through the FC characteristic test platform shown in Figure 2. Table 1 shows the results of the normal operation range, which has an average cell voltage of 0.6~0.8 V. It is mentioned that the lookup table in Figure 1 is constructed from the data in Table 1.

Table 1. Fundamental operating variables vector under different i_{stk} conditions.

i_{stk} (A/cm^2)	$\mathbf{X^0} = (\lambda^0_{ca}, RH^0_{ca}, \lambda^0_{an}, RH^0_{an}, P^0_{stk}, T^0_{stk})$						V_{FC}
	λ^0_{ca}	RH^0_{ca} (%)	λ^0_{an}	RH^0_{an} (%)	P^0_{stk} (kPa)	T^0_{stk} (°C)	
0.3	2.8	50	2.5	50	30	66	0.772
0.4	2.8	48	2.4	48	40	66	0.743
0.5	2.6	47	2.2	47	50	67	0.732
0.6	2.4	46	2.0	46	60	68	0.717
0.7	2.3	44	1.9	44	70	68	0.704
0.8	2.2	43	1.8	43	90	68	0.697
0.9	2.1	42	1.7	42	100	68	0.684
1.0 *	2.0	40	1.6	40	110	70	0.672
1.1	2.0	38	1.6	38	120	70	0.658
1.2	2.0	37	1.5	37	130	70	0.6501
1.3	2.0	36	1.5	36	130	71	0.646
1.4	2.0	35	1.5	35	130	72	0.637
1.5	2.0	34	1.5	34	130	73	0.628
1.6	2.0	33	1.5	33	130	73	0.619
1.7	1.9	32	1.5	32	140	73	0.610

* i_{stk} = 1 A/cm^2 is set as the reference operating point.

The voltage performance of the FC stack under fundamental operating environment $\mathbf{X^0}$ is shown in Figure 4. In this paper, i_{stk} = 1 A/cm^2 is set as the reference operating point, for example, to demonstrate the proposed technology. According to Table 1, the corresponding fundamental operating variables at i_{stk} = 1 A/cm^2 are (λ_{ca}, RH_{ca}, λ_{an}, RH_{an}, P_{stk}, T_{stk}) = (2.0, 40%, 1.6, 40%, 110, 70).

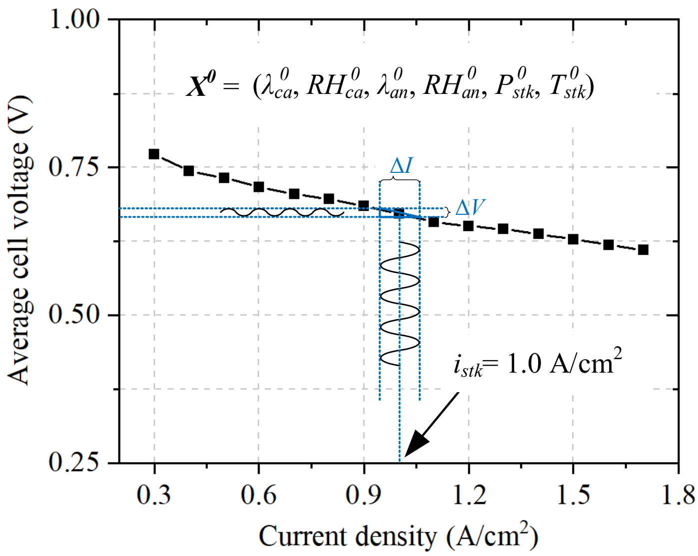

Figure 4. The voltage performance of the FC stack under the fundamental operating environment.

Since the operating variable vector of the stack has six dimensions, the steady-state response characteristic of the impedance is tested with the "One-way" Analysis Technique (which determines a variable's influence by the degree to which the objective function changes as that variable is varied while all other variables are held fixed) [45] to determine the impact of each independent operating variable on the impedance. The tested conditions are shown in Table 2. 34 groups of steady-state experiments of impedance spectrum will be carried out in this section. Except for the considered variable, other variables are maintained as fundamental values. Each test process measures the impedance spectrum after the stack's stable operation for 30 min.

Table 2. Impedance spectrum test scheme under steady-state conditions.

Variables	Basic Value	Test Conditions
λ_{ca}	2.0	1.8, 2.0, 2.2, 2.4, 2.6, 2.8
RH_{ca}	40%	0%, 20%, 40%, 60%, 80%, 100%
λ_{an}	1.6	1.2, 1.4, 1.6, 1.8, 2.0, 2.2
RH_{an}	40%	0%, 20%, 40%, 60%, 80%, 100%
P_{stk}	110 kPa	70, 90, 110, 130, 150
T_{stk}	70 °C	55, 60, 65, 70, 75

Figure 5 shows a typical impedance spectrum under fundamental conditions to explain the mechanism between the impedance spectrum and the internal operating state inside the stack. In Figure 5, the horizontal coordinate is the real part of the impedance, and the vertical coordinate is the negative imaginary part, represented by the area impedance $\Omega \cdot cm^2$. In the following sections of this paper, the measured impedances are the total value of the stack with 12 cells.

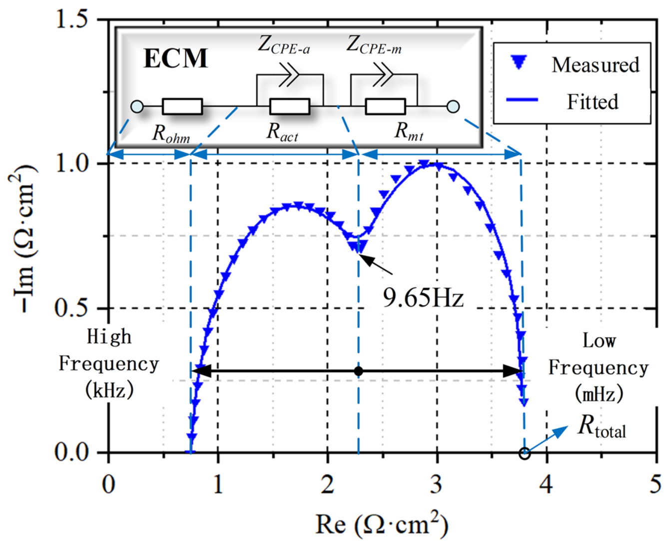

Figure 5. Impedance spectrum and its equivalent circuit model at fundamental conditions.

According to Figure 5, the intersection of the high-frequency (HF) (≥300 Hz) part and the real axis indicates that the stack has a pure resistance characteristic at this frequency, and the real axis intercept represents the magnitude of the ohmic resistance R_{ohm}. Ohmic resistance is mainly composed of electronic resistance and ionic resistance. The electron resistance is generated by the conduction of electrons in the electrode, bipolar plate, current collecting plate, and external wire, and the ion resistance is caused by the transport of protons in the PEM. In general, the electronic resistance remains unchanged with the change in operating conditions. The ionic resistance is closely related to the internal operating state (especially the membrane water content). The ionic resistance increases sharply when the membrane water content is very low. When the membrane is well hydrated, the ohmic resistance is almost equal and is not affected by changes in operating conditions.

The medium-frequency (MF) part (300~9.65 Hz) in Figure 5 represents the stack's activation process of the anode and cathode. There is an activation overvoltage in both the anode and cathode of the FC. The hydrogen oxidation reaction at the anode is very fast (meaning a higher characteristic frequency), and the oxygen reduction reaction at the cathode is relatively slow (meaning a lower characteristic frequency). The voltage drop caused by the activation loss mainly depends on the cathode reaction conditions. For the impedance spectrum shown in Figure 5, the impedance arc of anode activation is not obvious (challenging to distinguish in the arc segment close to the real axis). Thus, anode activation resistance can be ignored and simplified in the analysis, and the cathode activation resistance is represented by R_{act}.

The low-frequency (LF) part (9.65~0.1 Hz) in Figure 5 characterizes the mass transfer process inside the FC. The mass transfer process is much slower than electronic/ionic conduction and electrochemical reactions, and thus is reflected as the impedance in the LF band. The mass transfer impedance is denoted by R_{mt}. Since the reaction gas at the anode is high-purity hydrogen and the products (H_2O) are mainly produced in the cathode, it is the cathode operating conditions that mainly affect the LF impedance arc. At high current density, the generated water vapor leads to a decrease in the concentration of the reactants and an increase in the mass transfer impedance. In addition, the presence of liquid water further hinders the transportation of the reactants, increasing mass transfer losses.

The aforementioned impedance characteristic parameters, such as ohmic, activation, and mass transfer, characterize the operating state inside the FC stack and can be used as the original data to identify the operating state. To identify the impedance characteristic parameters, the impedance spectrum data in this paper are fitted using the equivalent circuit model (ECM) shown in Figure 5. The Constant Phase Element (CPE) is used to model the non-uniformly distributed double-layer capacitance effect. The impedance expression of the CPE is expressed by Equation (2):

$$Z_{CPE} = \frac{1}{Y_0(j\omega)^N} \tag{2}$$

where Y_0 is the capacitance coefficient of CPE, and N is the parameter to express the uniformity of the electrode surface. The value of N generally ranges from 0.5 to 1, and the larger the value of N, the higher the uniformity of the electrode surface [46]. When N = 1, the CPE module behaves as an ideal capacitor, and the capacitance value is Y_0.

At very low frequency ($\omega \rightarrow 0$), the real part of impedance can be regarded as the total resistance $R_{total} = R_{ohm} + R_{act} + R_{mt}$. In another way, the total resistance R_{total} is the intersection of the extension line of the LF impedance arc and the real axis in Figure 5. Moreover, the total resistance is precisely related to the inverse slope of the polarization curve in Figure 4.

By fitting the measured impedance data with the ECM structure shown in Figure 5, the values of R_{ohm}, R_{act}, $Z_{CPE\text{-}a}$, R_{mt}, and $Z_{CPE\text{-}m}$ can be obtained. The ECM structure adopted in this paper can obtain a good result with a Chi-square error of 10^{-4} orders. Then, by substituting model values into the ECM structure, the model and the fitted EIS curve (as shown in Figure 5) can also be obtained. Impedance data quantified by ECM will facilitate characteristic analysis in the following sections.

4.2. Results of EIS Measurement Under Steady-State Conditions

(1) Cathode air stoichiometric ratio λ_{ca} and cathode air humidity RH_{ca}

The EIS measured by varying the cathode operating conditions (λ_{ca} and RH_{ca}) at the fundamental operating point is shown in Figure 6. The EIS is presented in the form of Nyquist plots and Bode plots. From Figure 6a, it can be seen that the EIS pattern of the stack changes significantly with the change of λ_{ca}. From the perspective of FC electrochemical reaction kinetics, λ_{ca} mainly affects the reactant concentration and the drainage ability of the product (liquid water) [2,47]. When λ_{ca} increases, the concentration of oxygen involved in the electrochemical reaction increases. At the same time, the drainage capacity of the stack is also enhanced, which improves the mass transfer capacity and decreases the mass transfer impedance. In addition, the increase in λ_{ca} positively affects the cathode activation impedance. Thus, total impedance, activation impedance, and mass transfer impedance decrease monotonically with the increase in λ_{ca}. In particular, it should be noted that in extreme cases (low current density, high stack temperature), excessive λ_{ca} will lead to membrane drying, causing a sharp increase in ohmic impedance.

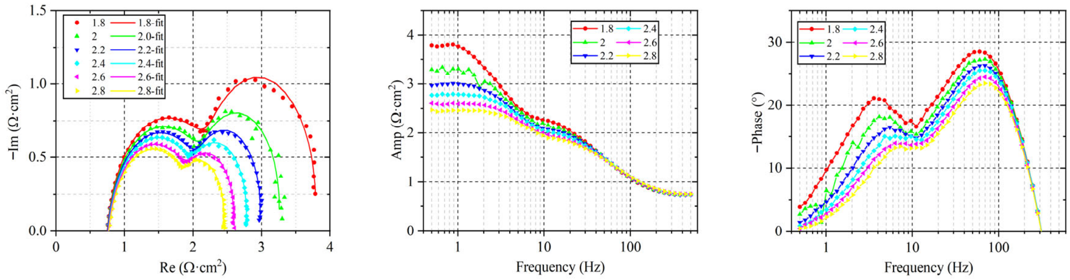

(**a**) Cathode air stoichiometric ratio λ_{ca}

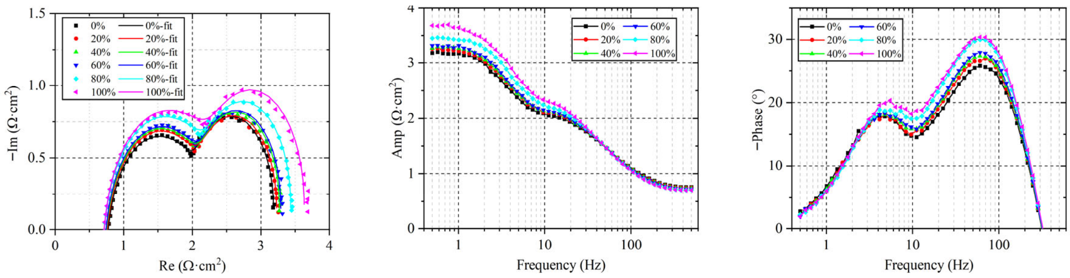

(**b**) Cathode air humidity RH_{ca}

Figure 6. Impedance measurement results under different cathode operating conditions. (**Left**) Nyquist plots, (**Middle**) amplitude-frequency characteristics of Bode plots, (**Right**) phase-frequency characteristics of Bode plots.

As seen from Figure 6b, the impedance spectrum of the stack also changes obviously with RH_{ca}. The humidity of the cathode inlet air mainly affects the hydration state of the membrane [48]. When the hydration of the membrane is low, the ohmic impedance increases. Due to the high fundamental operating current density (which means more H_2O production) of this experiment, no significant ohmic impedance increase is observed under low-humidification conditions. When the stack's humidity rises, the concentration of produced water vapor increases, the oxygen concentration in the flow channel decreases, and the difficulty of cathode reactant diffusion increases. Excessive liquid water may block the flow channel and gas diffusion layer pores, increasing activation and mass transfer impedance in this situation.

(2) Anode hydrogen stoichiometric ratio λ_{an} and anode hydrogen humidity RH_{an}

The EIS measured by changing the anode operating conditions (λ_{an} and RH_{an}) at the fundamental operating point is shown in Figure 7. When the λ_{an} varies from 1.2 to 2.2 in a wide range, the overall impedance value only changes in a small range and with no noticeable tendency. The results show that the change of λ_{an} does not affect the impedance characteristics of the stack, and the experimental results in this paper are consistent with the theoretical analysis results in the literature [2]. According to Figure 7b, when the cathode of the stack has good humidification conditions (the cathode air humidity is

40% and the stack is running at high current density), the change of the RH_{an} also does not bring significant changes in the impedance spectrum due to the good water permeability of PEM. At high current density operation, however, it is necessary to be alert to the accumulation of liquid water in the anode flow channel due to the high humidity of the inlet gas, which may lead to flooding failures.

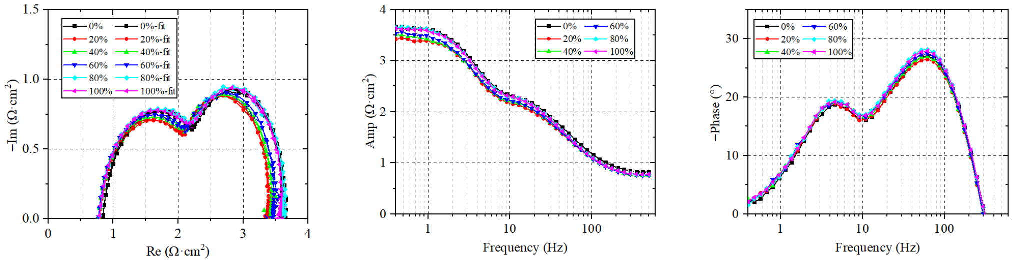

(**a**) Anode hydrogen stoichiometric ratio λ_{an}

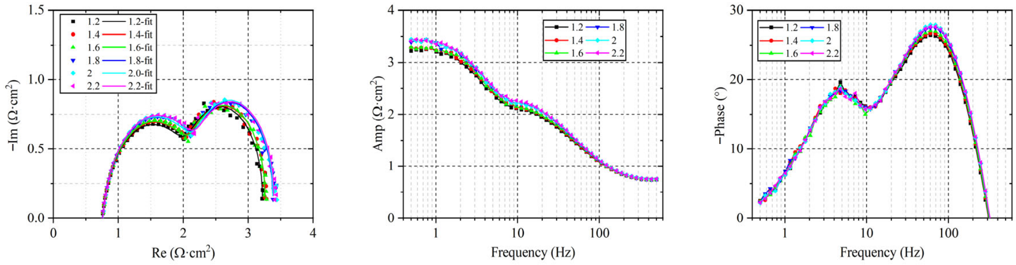

(**b**) Anode hydrogen humidity RH_{an}

Figure 7. Impedance measurement results under different anode operating conditions. (**Left**) Nyquist plots, (**Middle**) amplitude-frequency characteristics of Bode plots, (**Right**) phase-frequency characteristics of Bode plots.

(3) Stack operating pressure P_{stk} and temperature T_{stk}

The EIS measured by varying the stack operating conditions (P_{stk} and T_{stk}) at the fundamental operating point is shown in Figure 8.

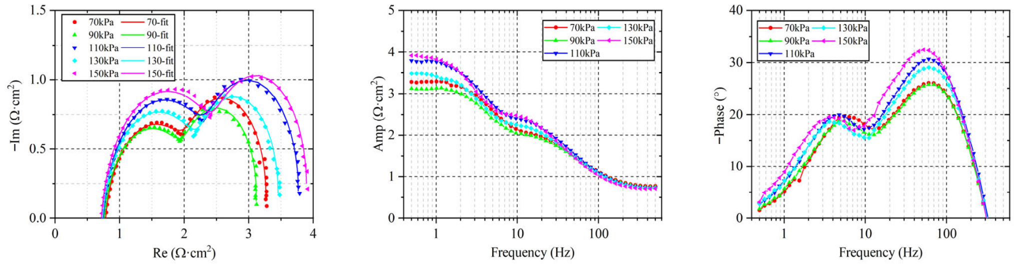

(**a**) Stack operating pressure P_{stk}

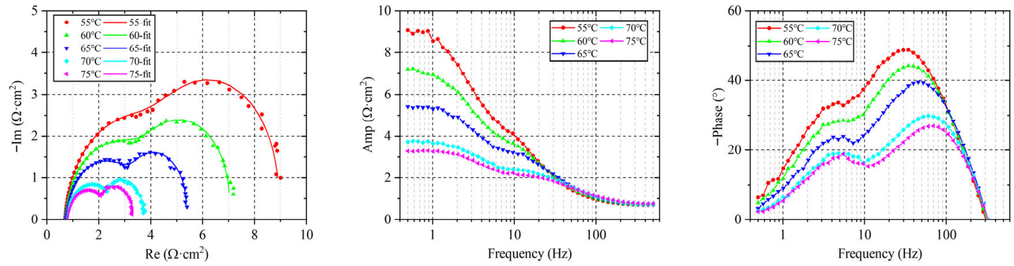

(**b**) Stack operating temperature T_{stk}

Figure 8. Impedance measurement results under different stack operating conditions. (**Left**) Nyquist plots, (**Middle**) amplitude-frequency characteristics of Bode plots, (**Right**) phase-frequency characteristics of Bode plots.

Stack operating pressure P_{stk}: When the inlet gas pressure is raised, the exchange current density will be increased, which can reduce the activation loss and activation impedance. In addition, the increased pressure facilitates the diffusion of gas from the flow channel to the catalytic layer, improving the mass transfer ability in the flow channel. However, when P_{stk} is increased, the gas flow rate will be reduced under the same total inlet mass flow, which is not conducive to the discharge of liquid water and may cause an increase in mass transfer losses. As a result of the positive and negative influences mentioned above, the EIS in Figure 8a varies irregularly.

Stack operating temperature T_{stk}: As shown in Figure 8b, when the T_{stk} increases, the activation impedance and mass transfer impedance decrease significantly. As the temperature rises, the gas molecule becomes more active which will accelerate the transport of oxygen in the diffusion layer and the catalyst layer, and the liquid water can be removed easily due to the reduced surface tension of the interface between the liquid water and the electrode material; as a result, the mass transport impedance will decrease as the temperature increases [49]. Furthermore, the catalyst's kinetics become faster as the temperature increases, which makes the charge transfer happen more quickly. So, the activation impedance gradually decreases as the temperature of T_{stk} increases.

4.3. Impedance Analysis Under Steady-State Conditions

(1) Sensitivity analysis

It is clear from the previous analysis that different operating variables have various degrees of influence on the EIS. To quantify the impact of each operating variable on EIS, this paper defines the maximum total impedance change under the proportional change of operating variables (defined as the normalized local sensitivity coefficient ζ [50]) to evaluate the sensitivity:

$$\zeta = (R_{total\text{-}max} - R_{total\text{-}min})/((\mathbf{X}_{max}(i) - \mathbf{X}_{min}(i))/\mathbf{X_0}(i)) \quad (3)$$

where $R_{total\text{-}max}$ and $R_{total\text{-}min}$ denote the maximum and the minimum value of the total impedance, respectively, $\mathbf{X_0}(i)$ represents the reference value of the ith operating variable in $\mathbf{X_0}$, $\mathbf{X}_{max}(i)$ and $\mathbf{X}_{min}(i)$ denote the maximum and the minimum value of $\mathbf{X}(i)$, respectively.

Based on the results of the previous experimental tests, the sensitivity coefficient ζ of each operating variable can be obtained as shown in Table 3. As can be seen from the table, the sensitivity of the stack for each operating variable is, in descending order, T_{stk}, λ_{ca}, P_{stk}, λ_{an}, RH_{ca}, and RH_{an}. In addition, the table also gives the maximum total impedance change that can be induced by each operating variable, which represents the impedance regulation ability of the corresponding operating variable, and the impedance modulation capability in descending order is T_{stk}, λ_{ca}, P_{stk}, λ_{an}, RH_{ca}, and RH_{an}.

It should be pointed out that the variation range of the operating variable given in the table represents the limit range of the controllable impedance under the operating condition. When the operating conditions exceed this range, the stack may be at significant risk of safety or cause the stack failure in stable operating conditions. According to Figure 7 and Table 3, due to the operating variables, RH_{an} and λ_{an} are insensitive to the impedance regulation of the stack and are not suitable as control variables for closed-loop management.

(2) Monotonicity and correlation analysis

Based on the above experimental results, the relationship between total impedance R_{total} and each operating variable $\mathbf{X}(i)$ is summarized, as shown in Figure 9. It can be seen from the figure that there is an apparent monotonic variation relationship between R_{total} and three operating conditions, λ_{ca}, RH_{ca}, and T_{stk}. The effect of the operating condition P_{stk} on R_{total} is bi-directional, and there is no monotonic relationship. Thus, to avoid evolving into a positive feedback system, P_{stk} is not suitable for the control variable of the closed-loop management system.

Table 3. Normalized local sensitivity coefficient ζ of different operating variables.

X(i)	$(X_{max}(i) - X_{min}(i))/X_0(i)$	$R_{total\text{-}max} - R_{total\text{-}min}$ ($\Omega\cdot cm^2$)	ζ
λ_{ca}	(2.8 − 1.8)/2 = 0.5	1.33	2.66
RH_{ca}	(100% − 0%)/40% = 2.5	0.45	0.18
λ_{an}	(2.2 − 1.2)/1.6 = 0.625	0.17	0.28
RH_{an}	(100% − 0%)/40% = 2.5	0.43	0.17
P_{stk}	(150 − 70)/110 = 0.727	0.77	1.06
T_{stk}	(75 − 55)/70 = 0.286	5.61	19.60

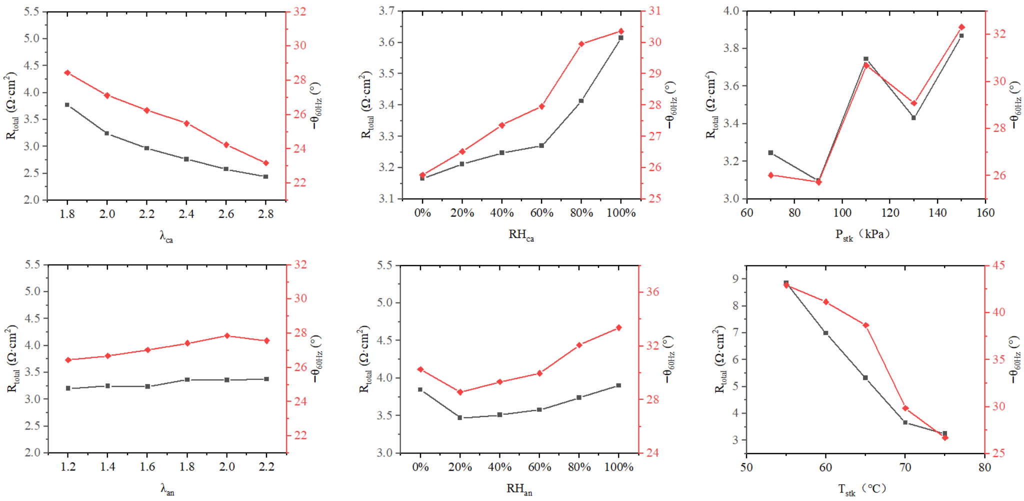

Figure 9. Relationship among X(i), Rtotal, and −θ60 Hz.

As mentioned above, R_{total} can effectively reflect the FC internal state. However, there are still some difficulties in practical application: R_{total} is obtained by measuring the impedance spectrum over a wide frequency range and then fitting by the ECM, which takes minutes to measure and calculate, and thus cannot be obtained in real time. Although the real part of the extreme LF impedance can be used to approximately characterize R_{total}, it also has the disadvantages of long measurement time (several tens of seconds) and large measurement error (susceptible to interference and cannot be corrected by complete spectrum data fitting).

By comparing the amplitude-frequency characteristics and phase-frequency characteristics in the Bode plots from Figure 6 to Figure 8, it can be found that the amplitude-frequency characteristics of extreme LF are correlated with the phase-frequency characteristics at MF (about 20~80 Hz). In other words, the impedance phase angle in MF can effectively reflect the R_{total} as well as the FC internal state. Therefore, the impedance phase angle of the MF can be used as a parameter to characterize the FC's internal operating state. Considering the rapidity of phase angle measurement and the resolution of state estimation, the impedance phase angle at 60 Hz (marked with $-\theta_{60Hz}$) is selected as the reference of the FC internal operating state and plotted to the right coordinate in Figure 9. Through the analysis of the two curves in Figure 9, it can be seen that the trend of $-\theta_{60Hz}$ is entirely consistent with R_{total}. It should be specially pointed out that other frequencies within the range of 20~80 Hz can also be used to identify the internal state of the stack. In addition, the grid frequency in the author's home country is 50 Hz, so the selection of 60 Hz will avoid interference from the power grid.

To further demonstrate the correlation between the R_{total} and $-\theta_{60Hz}$, the correlation analysis method in the field of statistics is introduced. The Pearson Correlation Coefficient

(PCC) is used to measure the correlation between two sets of data from different sources [51]. When the correlation coefficient is bigger than 0.9, the two data sets are considered strongly correlated. The PCC is calculated as follows:

$$\rho_{R,\theta} = \frac{Cov(R,\theta)}{\sigma_R \sigma_\theta} \tag{4}$$

where R and θ are n-dimensional data variables, denoting the n sets of R_{total} and $-\theta_{60Hz}$ in this paper. σ_R and σ_θ are the standard deviations of R and θ, respectively, and Cov(R, θ) is the covariance between them. The covariance is calculated by the following formula:

$$Cov(R,\theta) = \frac{\sum_{i=1}^{n} (R(i) - \overline{R})(\theta(i) - \overline{\theta})}{n-1} \tag{5}$$

Considering that the closed-loop management strategy adopts a minor correction $\mathbf{\Delta X}$ on the fundamental operating conditions $\mathbf{X^0}$ (as shown in Figure 1), the R_{total} of the FC stack under the fundamental operating environment is around 3.5~3.8 $\Omega{\cdot}cm^2$. Given that the stack operates at a temperature of above 65 °C under normal conditions, the two temperature values of 55 °C and 60 °C, which are lower than the normal operating temperature, can be excluded from the analysis. Therefore, the two values of R_{total} that deviate significantly (bigger than 6 $\Omega{\cdot}cm^2$ @ T_{stk} = 55, 60 °C) can be removed, and the R_{total} measured in 32 sets of experiments can be summarized. By substituting R_{total} and $-\theta_{60Hz}$ into the above Formulas (4) and (5), the PCC can be obtained as 0.9596. This result indicates that $-\theta_{60Hz}$ has a significant positive correlation with R_{total}.

The relationship curve obtained by data fitting between R_{total} and $-\theta_{60Hz}$ is shown in Figure 10, and the linear relationship between the two parameters is $-\theta_{60Hz}$ = 9.4 + 5.5 × R_{total}. Therefore, the R_{total} can be estimated by measuring the phase angle $-\theta_{60Hz}$. Compared with the measurement of the total impedance R_{total}, the MF impedance phase angle $-\theta_{60Hz}$ measurement has the advantages, as shown in Figure 10.

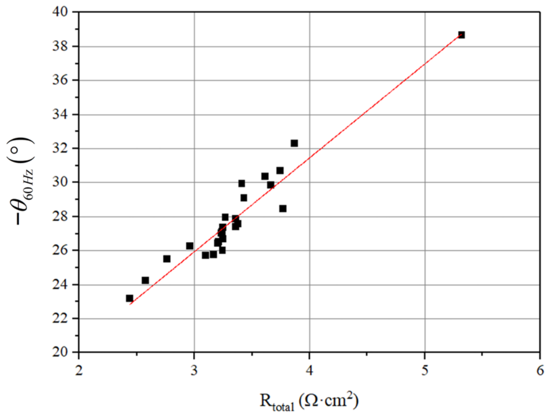

Figure 10. Linear relationship between R_{total} and $-\theta_{60Hz}$.

Fast measurement speed: Fourier transform-based methods [38,52] generally require data in one signal period to calculate the impedance phase for a given frequency. Considering the demand for multi-period smoothing to obtain a stable feedback signal, the measurement time of $-\theta_{60Hz}$ can achieve less than 100 ms.

High measurement accuracy: Referring to the grid voltage phase angle measurement technology in the field of power electronics, the steady-state error of phase measurement is almost zero, and it can achieve less than 0.6° under dynamic operating conditions [53].

High estimation resolution: According to those abovementioned linear fitting results, the amount of impedance phase change is 5.5° for a total impedance change of 1 Ω·cm^2.

The wide variation range, combined with high measurement accuracy and resolution, allows for high estimation accuracy. Thus, the $-\theta_{60Hz}$ meets the requirement for rapidity, accuracy, and validity of the feedback parameter used for closed-loop management. It should be additionally noted that the slope and intercept values are stack-specific and should be recalibrated for different stack designs, materials, or operating conditions.

(3) Impedance characteristics analysis under fault conditions

The above conclusions are based on the EIS analysis under appropriate operating conditions. However, flooding and membrane drying failures are two kinds of frequent failures. Moreover, adjusting water content in the FC stack is the main task of closed-loop management. Figure 11 shows the EIS characteristics for two typical failures, which are used to check the validity of R_{total} and $-\theta_{60Hz}$ as feedback parameters for the stack internal state estimation.

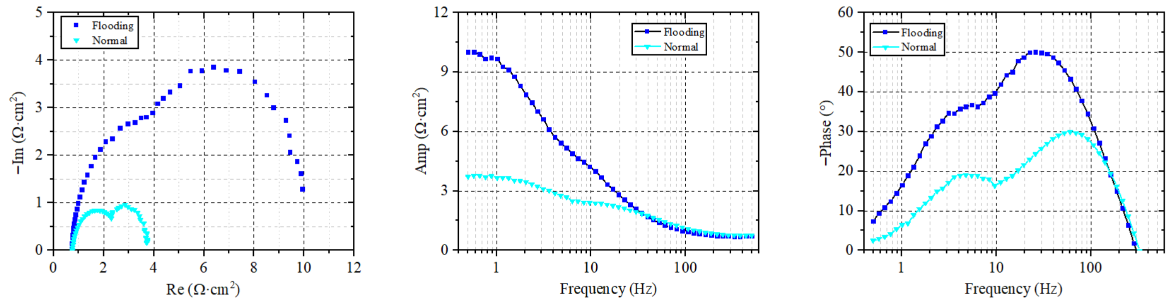

(**a**) Flooding and normal conditions @1.0 A/cm²

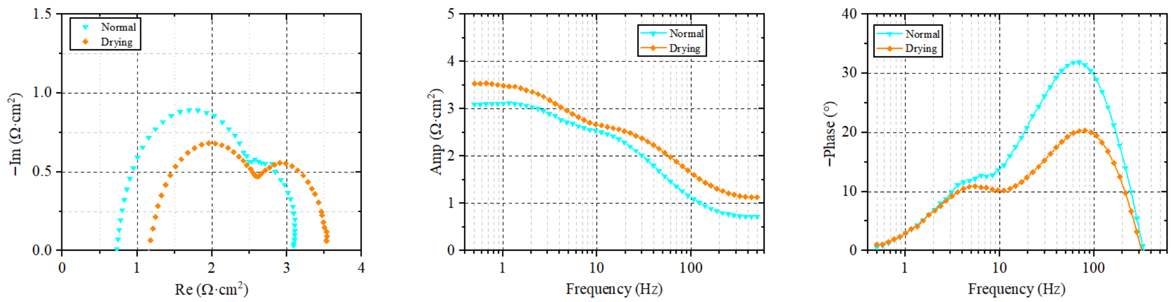

(**b**) Membrane drying and normal conditions @0.6 A/cm²

Figure 11. Impedance measurement results under typical faults. (**Left**) Nyquist plots, (**Middle**) amplitude-frequency characteristics of Bode plots, (**Right**) phase-frequency characteristics of Bode plots.

Figure 11a shows the impedance measurement results of flooding fault and normal conditions. The flooding fault is obtained in the conditions of high current density (1 A/cm^2), low λ_{ca} (1.6), low T_{stk} (50 °C), and high RH_{ca}. It can be seen from the figure that when the FC is flooding, the ohmic impedance remains unchanged, and the activation and mass transfer impedance increase significantly. The shape of the impedance spectrum is similar to that shown in Figures 6–8. Thus, the results obtained from Figures 6–8 are still practical. The two parameters (R_{total} and $-\theta_{60Hz}$) can also be used as internal operating state estimation.

Figure 11b shows the impedance measurement results of the membrane drying fault and normal conditions. The membrane drying fault is obtained in the conditions of low current density (0.6 A/cm^2), high λ_{ca} (3.0), high T_{stk} (T_{stk} = 75 °C), and low RH_{ca}. It can be seen from the figure that when the membrane drying fault occurs in the stack, the activation and mass transfer impedance remain unchanged, and the ohmic impedance increases significantly. According to the amplitude-frequency characteristics, the variation trend of LF impedance under the membrane drying condition is the same as that under the flooding fault. Therefore, relying solely on LF impedance cannot distinguish a membrane drying fault from a flooding fault and cannot conduct correct and effective closed-loop regulation. The existing literature approach distinguishes drying and flooding faults by combining HF and LF impedance [42]. In particular, analysis of the phase-frequency characteristics in Figure 11b shows that the membrane drying fault and the flooding fault have opposite variation trends from the normal state in the MF band. Thus, it is very easy to distinguish between these two faults from the normal state using the MF phase angle $-\theta_{60Hz}$. Taking i_{stk} = 1 A/cm^2 for example, the following criteria can be used to diagnose faults: when $-\theta_{60Hz} > 40°$, it is the flooding fault; when $-\theta_{60Hz} < 25°$, it is the membrane drying fault. It should be noted that this diagnostic rule requires calibration under other current density conditions.

(4) Validation of the phase angle of the MF impedance $-\theta_{60Hz}$

Based on the previous analysis, it can be seen that the MF impedance phase angle $-\theta_{60Hz}$ is of great value in identifying the internal operating state of the FC stack, and its applicability will be analyzed below by combining $-\theta_{60Hz}$ with the closed-loop management method in Figure 1. In this paper, we define the operation state factor S_{stk} in Figure 1 to be equal to $-\theta_{60Hz}$, and the value of 29~31° can be used as the target value. Temporarily, S^*_{stk} = 30° is selected as the target value under the fundamental operating point. Three parameters T_{stk}, λ_{ca}, and RH_{ca} can be used as control variables for closed-loop management (other operating conditions remain at fundamental values), and the control directions under different internal states S_{stk} are obtained, as shown in Table 4.

Table 4. The direction of regulation for closed-loop management under different operating conditions.

Conditions	$S_{stk} = -\theta_{60Hz}$	T_{stk}	λ_{ca}	RH_{ca}	Evidence
No faults	$S_{stk} > S^*_{stk}$, $S^*_{stk} - S_{stk} < 0$	↑	↑	↓	Figures 5 and 7b
	$S_{stk} < S^*_{stk}$, $S^*_{stk} - S_{stk} > 0$	↓	↓	↑	Figures 5 and 7b
Flooding fault	$S_{stk} > S^*_{stk}$, $S^*_{stk} - S_{stk} < 0$	↑	↑	↓	Figure 11a
Membrane Drying fault	$S_{stk} < S^*_{stk}$, $S^*_{stk} - S_{stk} > 0$	↓	↓	↑	Figure 11b

↑, increase the parameter; ↓, decrease the parameter.

Based on the monotonic relationship between $S_{stk} = -\theta_{60Hz}$ and the control variable in Figure 9, the control direction can be determined under no fault. When S_{stk} is greater than S^*_{stk}, the total impedance of the current operation condition is too large, indicating that the closed-loop control strategy needs to be adjusted to the direction of making S_{stk} decrease. At this time, we can increase the T_{stk} (increase the activity of the catalyst, increase the gas diffusion coefficient, and accelerate the gas transport), increase the λ_{ca} (increase the concentration of reactants), and decrease the RH_{ca} (reduce the water vapor concentration to increase the reactant concentration) to make S_{stk} decrease. Similarly, when the operating state feedback S_{stk} is less than the target value S^*_{stk}, these three control variables are regulated in opposite directions, as shown in Table 4.

When the flooding fault occurs, S_{stk} will be much larger than S^*_{stk}, and the closed-loop control strategy needs to be adjusted to the direction of S_{stk} reduction (refer to Figure 11a), which requires increasing the λ_{ca}, increasing the T_{stk}, and reducing the RH_{ca}. Compared with the aforementioned experimental conditions of flooding fault, it can be easily observed that the regulation operation direction is correct and will be effective. Increasing the λ_{ca} enhances the ability of the cathode gas to bring out liquid water, increasing the T_{stk} reduces the ability of reacting products to convert into liquid water, and reducing the RH_{ca} reduces the water brought in from outside. All three measures above are conducive to recovering the FC stack from the flooding fault.

When the membrane drying fault occurs, S_{stk} will be much smaller than S_{stk}^*. The closed-loop control strategy needs to be adjusted to the direction of S_{stk} increase (refer to Figure 11b), so the λ_{ca} needs to be reduced, the T_{stk} needs to be lowered, and the RH_{ca} of the inlet gas needs to be increased. Compared with the aforementioned conditions for constructing the membrane drying fault, it can be easily obtained that the direction of the adjustment is correct and will be effective. All three measures will help the stack to recover from the membrane drying fault.

In summary, using the operating state factor S_{stk} constructed by the MF impedance phase angle $-\theta_{60Hz}$ can not only identify the fault state but also sense the improper operating state in the non-fault state, such as a too-low operating temperature (T_{stk} = 55, 60 °C, refer to Figure 8b), too-low cathode stoichiometric ratio (λ_{ca} = 1.8, refer to Figure 6a), etc. In addition, when the operating state factor S_{stk} deviates from the target value S_{stk}^*, the regulation direction made by the closed-loop management strategy will not change for fault and non-fault states, which facilitates the design of the control strategy.

5. Analysis of Dynamic Response Characteristics Based on Impedance Phase Angle Measurement

5.1. Impedance Testing Scheme in Dynamic Conditions

After analyzing the impedance steady-state response characteristics in Section 4, the validity of using the $-\theta_{60Hz}$ as the internal operating state S_{stk} feedback parameter of the stack was demonstrated. In addition, three optimal operating conditions, T_{stk}, λ_{ca}, and RH_{ca}, could be selected as control variables for closed-loop management. In the actual application system, the RH_{ca} is usually humidified by cathode outlet gas and cannot be independently regulated. Thus, RH_{ca} will not be used as a control variable in the following sections.

In this section, the dynamic response characteristics of the internal operating state S_{stk} will be evaluated by changing two preferred operating variables. Similarly, the dynamic response characteristics of S_{stk} are also tested using the “One-way” Analysis Technique, and the operating conditions at 1 A/cm^2 are also defined as the reference conditions. The single-factor test conditions are shown in Table 5, and the impedance phase angle $-\theta_{60Hz}$ is also measured by the equipment in Figure 3. The difference with the steady-state test is that the perturbation current frequency of the programmable electronic load in this experiment is set as the fixed frequency of 60 Hz.

Table 5. Impedance phase angle test scheme under dynamic conditions.

Conditions	Fundamental Value	Test Conditions
λ_{ca}	2.0	2.0 → 1.8, 2.0 → 2.4
T_{stk}	70 °C	70 → 65, 70 → 75

→, left side: operating variables before dynamic adjustment; right side: operating variables after dynamic adjustment.

5.2. Results and Analysis of Dynamic Response Characteristics

(1) Cathode air stoichiometric ratio λ_{ca}

Figure 12a shows the dynamic response characteristics of stack internal state S_{stk} when the λ_{ca} is reduced to 1.8 from the reference value 2.0. In the FC stack test bench shown in Figure 2, the λ_{ca} is changed by the air supply subsystem’s MFC, the air mass flow adjustment process is very rapid, and the adjusting time is less than 3 s, as shown in Figure 12a. The response time of S_{stk} to the change of λ_{ca} is less than 2 s. In summary, when λ_{ca}^* negative step, the response time from λ_{ca}^* to λ_{ca} is about 3 s, the response time from λ_{ca} to S_{stk} is about 2 s, and the total response time from λ_{ca}^* to S_{stk} is about 5 s.

https://doi.org/10.3390/en19041049

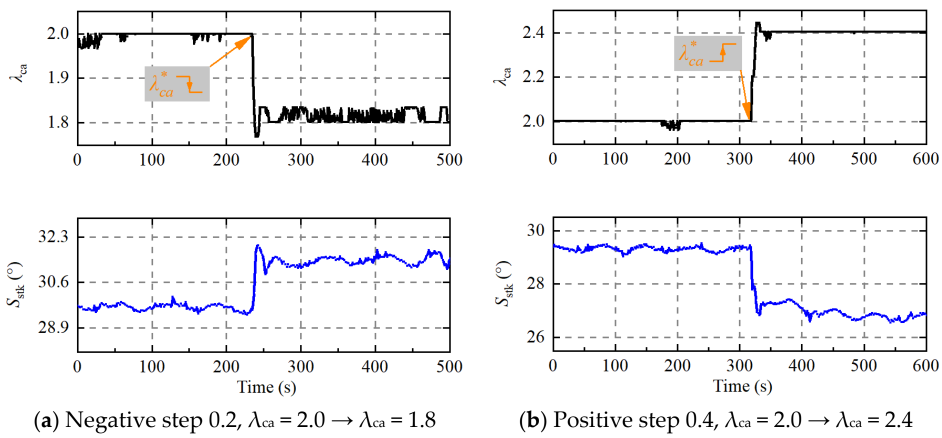

Figure 12. Dynamic response characteristics for varying cathode air stoichiometric ratio λ_{ca}.

Figure 12b shows the dynamic response characteristics of stack internal state S_{stk} when increasing the λ_{ca} from the reference value of 2.0 to 2.4. Analysis of the test data shows that the response time for adjusting the λ_{ca} is about 10 s (the MFC contains a flow rate closed-loop control system with the flow meter measurement as feedback and the proportional valve as an actuator unit). The response time of S_{stk} to the change of λ_{ca} is also less than 2 s. In summary, when λ_{ca}^* positive step, the response time from λ_{ca}^* to λ_{ca} is about 10 s, the response time from λ_{ca} to S_{stk} is about 2 s, and the total response time from λ_{ca}^* to S_{stk} is about 12 s.

(2) Stack operating temperature T_{stk}

Figure 13 shows the dynamic response characteristics of S_{stk} under the stack operating temperature T_{stk}, with negative and positive steps. It can be seen from the figure that when T_{stk} changes, the measured S_{stk} quickly follows the change because the T_{stk} can affect the rate of electrochemical reactions. After the temperature reaches its steady-state value, the temperature will continue to affect the balance of the water in the stack. Therefore, the S_{stk} continues to change slowly until a new balance is reached. The temperature adjustment time of the negative step 5 °C is about 200 s, and the temperature adjustment time of the positive step 5 °C is about 150 s. The difference between positive and negative temperature adjustment time depends on the difference between heating and cooling power in the FC stack test bench. After the temperature reaches its target value, the water balance time is about 350 s.

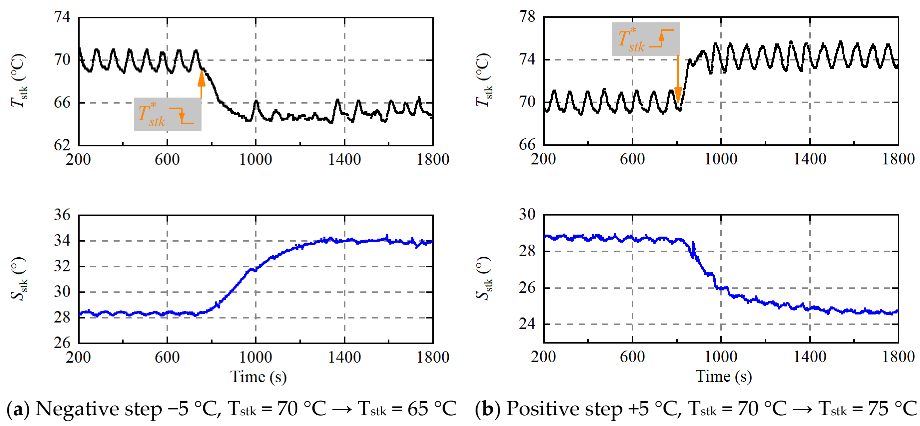

Figure 13. Dynamic response characteristics for varying stack operating temperature T_{stk}.

(3) Discussion and analysis

From the previous analysis results, it is clear that $-\theta_{60Hz}$ can provide continuous, dynamic, and fast feedback on the internal operation state S_{stk} of the stack. The results of the aforementioned impedance dynamic characteristic are summarized as shown in Table 6.

Table 6. Experimental results in the dynamic response characteristics test.

	X*(i) to X(i)	**X(i) to S_{stk}**	**X*(i) to S_{stk}**
λ_{ca}	Regulated by MFC, very fast, 3 s@−0.2, 10s@+0.4.	It mainly influences electrochemical reactions, very fast, about 2 s.	Very fast, in order of 10 s
T_{stk}	Regulated by the temperature of stack inlet coolant, very slow, 150 s@+5 °C, 200 s@−5 °C.	First stage: mainly influences electrochemical reaction, very fast, about 2 s. Second stage: mainly influences water balance, very slow, about 350 s.	Very slow, in order of 500 s

It can be seen from Table 6 that the time required to adjust the target condition (from **X***(i) to **X**(i)) for the auxiliary subsystem varies widely. The response time from λ^*_{ca} to S_{stk} is speedy and in the order of 10 s. In addition, the influence of input condition T_{stk} on S_{stk} includes two parts: one part is related to the electrochemical reactivity of the stack, and another part correlates with the state of water balance inside the FC stack. The effect of operating conditions on the reactivity of the stack is very rapid, and its response time is about 2 s, while the water balance process is slow, with a response time of about 350 s. The time constant of the dynamic process measured in this section can provide a robust basis for the parameter design of a closed-loop management strategy.

6. Application of Internal State Estimation Technology in System Closed-Loop Management

According to the above steady and dynamic analysis results, this section applies the estimated stack internal state S_{stk} into closed-loop management. The block diagram of the closed-loop management strategy is shown in Figure 14. The FC stack test bench can be treated as the FC system, which consists of an FC stack and three auxiliary subsystems. The control strategy is implemented in system monitoring and management software. The internal state S_{stk} ($-\theta_{60Hz}$) is measured by a TMS320F28335 board with a signal processing circuit. In this paper, the Second-Order Generalized Integrator (SOGI) algorithm [54] is used to calculate the phase angle. The measured S_{stk} is fed back to the monitoring and management system by RS232 serial port communication. In this paper, the cathode air stoichiometric ratio λ_{ca} and the stack operating temperature T_{stk} are separately used as regulatory variables to regulate the internal operating state of the stack to verify its effectiveness. These two strategies have similar control block diagrams. Their differences are control variables (λ_{ca} or T_{stk}) and controller parameters.

Green: by adjusting the cathode air stoichiometric ratio λ_{ca}. Orange: by adjusting the stack operating temperature T_{stk}.

6.1. By Adjusting the Cathode Air Stoichiometric Ratio λca

To verify the effectiveness of λ_{ca} in adjusting the FC stack's internal operating state, experiments of closed-loop management were carried out under the reference operating conditions of 1.0 A/cm^2. The fundamental operating conditions in the experiment were set as $\mathbf{X}^0 = (\lambda^0_{ca}, RH^0_{ca}, \lambda^0_{an}, RH^0_{an}, P^0_{stk}, T^0_{stk})$ = (2.0, 40%, 1.6, 40%, 110, 70). According to the control block diagram shown in Figure 14, the internal state S_{stk} of the stack is measured by the estimation method proposed in this paper. The difference between it and the target state is obtained: $\Delta S = S^*_{stk} - S_{stk}$, and the offset of the cathode air stoichiometric ratio $\Delta\lambda_{ca}$ is calculated by the controller. According to the dynamic response analysis in Section 5.2, the controller adopts Proportional-Integral (PI) control with the proportional parameter

$K_{P\text{-}ca} = -1$ and integral parameter $K_{I\text{-}ca} = -0.5$. The period of closed-loop management is set as 0.5 s. Then, the offset $\Delta\lambda_{ca}$ is added to the fundamental value $\lambda^0_{ca} = 2.4$, and the result of $\lambda^*_{ca} = \lambda^0_{ca} + \Delta\lambda_{ca}$ is set as given instruction for air supply subsystems. Meanwhile, other operating conditions are maintained as the fundamental operating conditions. The experiment results are shown in Figure 15. The initial value of the reference state S^*_{stk} is set to 23.6°, then step change +2°@554s, +2°@1207 s, −2°@1875 s, −2°@2968 s, +2°@3911 s. As can be seen from the figure, when the reference state S^*_{stk} changes, the FC stack internal operating state S_{stk}, which is measured by impedance phase angle in real time, can be quickly tracked to the target value by adjusting the cathode air metering ratio λ_{ca}. The control error in the steady state is less than 0.2°. The closed-loop adjustment time for the dynamic process in a step change is about 40 s.

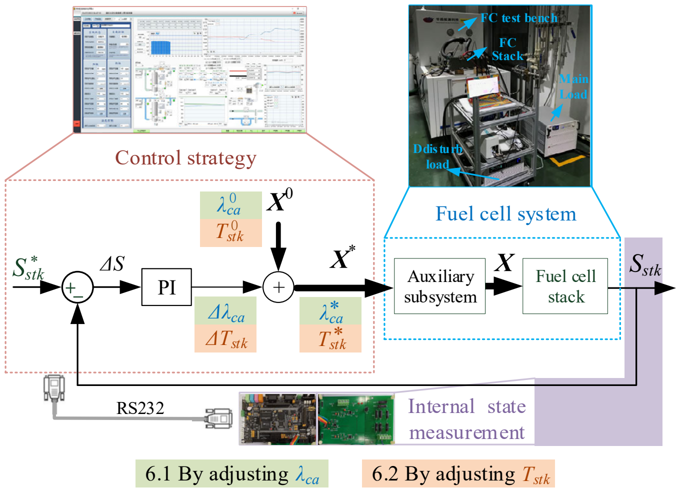

Figure 14. Closed-loop management strategy block diagram based on internal state S_{stk} feedback.

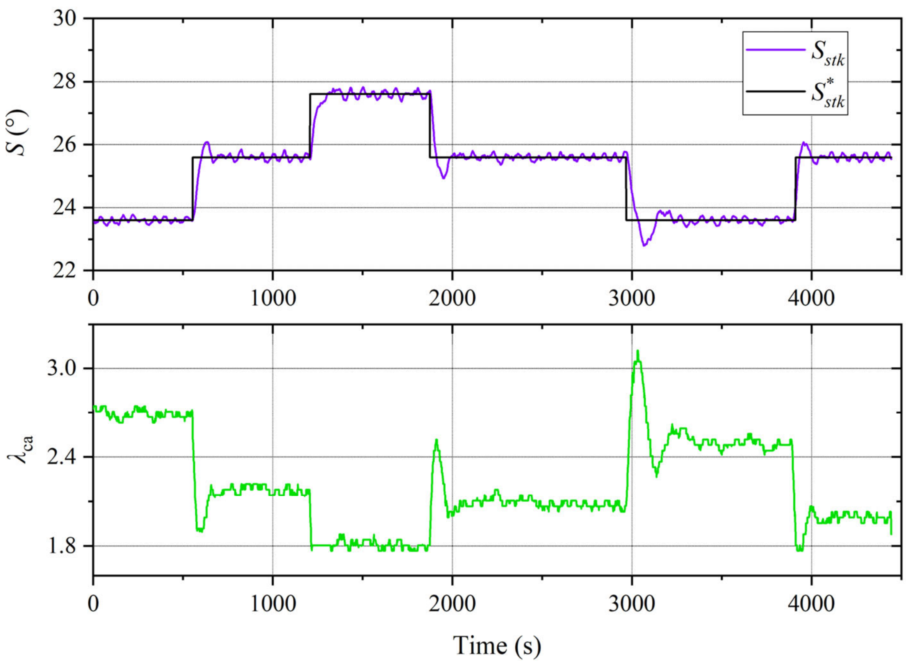

Figure 15. Experiment results of internal state closed-loop management by adjusting the cathode air stoichiometric ratio λ_{ca}.

6.2. By Adjusting Stack Operating Temperature T_{stk}

The experiment of internal state closed-loop management by adjusting T_{stk} is also based on the operating conditions of 1.0 A/cm^2 and the fundamental operating conditions of $\mathbf{X}^0 = (\lambda^0_{ca}, RH^0_{ca}, \lambda^0_{an}, RH^0_{an}, P^0_{stk}, T^0_{stk})$ = (2.0, 40%, 1.6, 40%, 110, 70). The control variable is stack operating temperature $T_{stk,}$ and the offset value ΔT_{stk} is obtained after the controller calculation. The controller also adopts Proportional-Integral (PI) control with the proportional parameter $K_{P\text{-}T\text{-}stk} = -0.5$ and integral parameter $K_{I\text{-}T\text{-}stk} = -0.5$. The period of closed-loop management is set as 20 s. Then, the offset ΔT_{stk} is added to the fundamental value $T^0_{stk} = 70$, and the result of $T^*_{stk} = T^0_{stk} + \Delta T_{stk}$ is set as given instruction for the thermal management subsystem. Meanwhile, other operating conditions are maintained as the fundamental operating conditions. The experiment results are shown in Figure 16. The initial value of the reference state S^*_{stk} is set to 23.6°, then step change +2°@681s, +2°@1910s, −2°@3218s, −2°@4308s. As can be seen from the figure, when the reference state S^*_{stk} changes, the FC stack internal operating state S_{stk} can be tracked to the target value by adjusting the stack operating temperature T_{stk}. According to the sensitivity analysis results in Section 4.3, the internal state is susceptible to T_{stk}. The control error in the steady state is determined by the control accuracy of T_{stk}. Because of the periodic oscillation of T_{stk}, the control error of S_{stk} in the steady state is about 0.3°. The temperature control of the thermal management subsystems in the test bench is very slow. Thus, the closed-loop adjustment time is more than 250 s in dynamic situations.

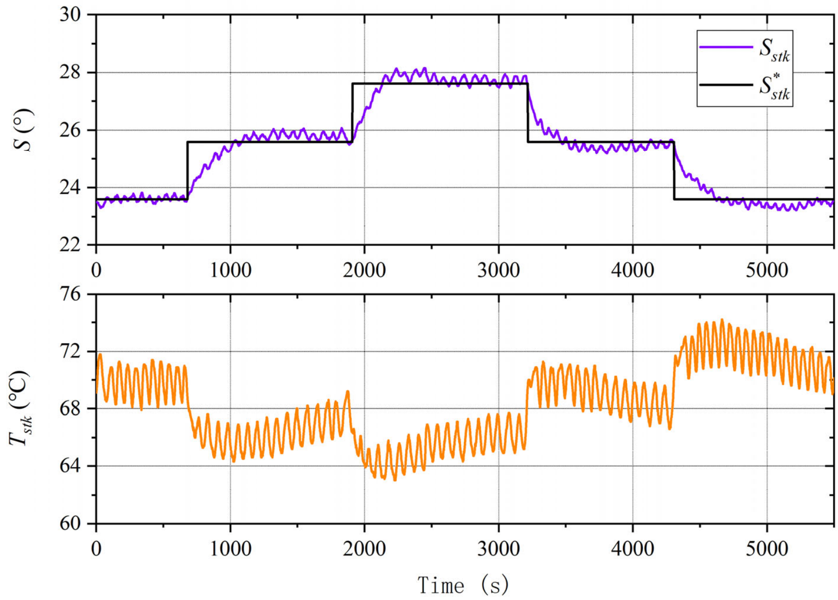

Figure 16. Experiment results of internal state closed-loop management by adjusting stack operating temperature T_{stk}.

6.3. Discussion

The experiment results show their effectiveness in managing FC stack internal state S_{stk} by adjusting cathode air stoichiometric ratio λ_{ca} and stack operating temperature T_{stk}. The performance comparisons of the two kinds of methods are summarized in Table 7. The adjustment of λ_{ca} has a minor steady-state error and shorter dynamic response time compared with adjusting T_{stk}. However, a more significant λ_{ca} means more power consumption for the air compressor. According to the statistical analysis of the 65-kW FC system under the condition of 1.0 A/cm^2 in [55], the air supply subsystem's power consumption accounts for 87% of the power losses of the three auxiliary subsystems, and the thermal management subsystem's power consumption accounts for 7% power losses. In addition, the air compressor is the air supply subsystem's main component for power consumption, thus, adjusting λ_{ca} cost more in electric power, and is suitable for rapid adjustment under emergency conditions. The adjustment of T_{stk} has the advantage of less power consumption and higher sensitivity, and is ideal for ordinary regulation.

Table 7. Performance comparisons of closed-loop management by adjusting cathode air stoichiometric ratio λ_{ca} and stack operating temperature T_{stk}.

	Steady State Error	Dynamic Response Time	Cost in Application
λ_{ca}	<0.2°	about 40 s	More power consumption for the air compressor when λ_{ca} ↑
T_{stk}	<0.3°	>250 s	More power consumption for the cooling fan when T_{stk} ↓

↑, increase the parameter; ↓, decrease the parameter.

The results of the closed-loop operation management method with FC stack internal state feedback based on single-frequency impedance phase angle measurement are feasible. In future applications, we can use the single-frequency impedance online measurement technology to identify the running state of the stack and define the proper state value of the system belonging to the "proper state." Once the measured value deviates from the "proper state," the FC system can recover from the "improper state" to the "proper state" by adjusting the preferred operation variable according to the urgency and severity of the deviation. With the proposed method, the system can be maintained in the most suitable state and avoid the "improper state" and faults as far as possible. This method gives expression to the idea of impedance shaping and can be helpful in system management to enhance the reliability and durability of the FC system.

7. Conclusions

To meet the requirements of closed-loop operation management of an FC system, the impedance response of an FC graphite plate stack with a reaction area of 330 cm^2 and 12 cells was investigated under steady-state and dynamic operating conditions in this paper. A fast estimation method of stack internal operating states based on the MF impedance phase angle was proposed and verified in the application. The main conclusions are as follows:

- The MF impedance phase angle $-\theta_{60Hz}$ can effectively estimate the internal operating state S_{stk} of the FC stack, including fault state and non-fault state (including inappropriate or improper operating).
- The measurement of MF impedance phase angle $-\theta_{60Hz}$ has the characteristics of fast measurement speed (within 100 ms), small measurement error (<±0.6°), and high state identification resolution (about $5.5°/\Omega\cdot cm^2$).
- When the feedback of the operating state factor ($S_{stk} = -\theta_{60Hz}$) deviates from the reference value, whether a fault or non-fault state, the direction of the regulation made by the closed-loop management system does not change, and the control system has formal consistency.
- Considering the evaluation indices such as sensitivity, regulation ability, monotonicity in impedance regulation, and feasibility in real systems, the optimal control variables suitable for closed-loop management are T_{stk} and λ_{ca}. Between them, the cathode air stoichiometric ratio λ_{ca} is faster to adjust the impedance, and the stack operating temperature T_{stk} has the widest adjustment range and the highest sensitivity to the state.
- By analyzing the step response characteristics of operation variables, the time constant of the dynamic process is measured. It can provide a robust basis for the parameter design of closed-loop operation management of the FC system.
- The experiment results show their effectiveness in managing FC stack internal state S_{stk} by adjusting cathode air stoichiometric ratio λ_{ca} and stack operating , thus,

adjusting λ_{ca} cost more in electric power, and is suitable for rapid adjustment under emergency conditions. The adjustment of T_{stk} has the advantage of less power consumption and higher sensitivity, and is ideal for ordinary regulation.

With the proposed FC internal state estimation and the closed-loop management method, the FC system can be maintained in the most suitable state and avoid the "improper state" and faults as far as possible. The proposed method gives expression to the idea of impedance shaping and will be helpful in system management to enhance the reliability and durability of the FC system.

Author Contributions: Conceptualization, K.L. and H.T.; methodology, W.N.; software, W.N.; formal analysis, W.N. and W.Z.; investigation, W.N., K.L., W.Z., and R.W.; resources, W.N., W.Z., and R.W.; writing—original draft, W.N.; writing—review and editing, K.L. and H.T.; supervision, H.T.; project administration, H.T.; funding acquisition, W.N. All authors have read and agreed to the published version of the manuscript.

Funding: This research was funded by the Chongqing Science and Technology Plan Project (No. CSTB2025TIAD-KPX0060).

Data Availability Statement: The raw data supporting the conclusions of this article will be made available by the authors on request.

Acknowledgments: This work was supported by the Chongqing Science and Technology Plan Project (No. CSTB2025TIAD-KPX0060).

Conflicts of Interest: The authors declare no conflict of interest.

References

1. Piras, M.; De Bellis, V.; Malfi, E.; Novella, R.; Lopez-Juarez, M. Adaptive ECMS based on speed forecasting for the control of a heavy-duty fuel cell vehicle for real-world driving. *Energy Convers. Manag.* **2023**, *289*, 117178. [CrossRef]
2. Rezaei Niya, S.M.; Phillips, R.K.; Hoorfar, M. Study of anode and cathode starvation effects on the impedance characteristics of proton exchange membrane fuel cells. *J. Electroanal. Chem.* **2016**, *775*, 273–279. [CrossRef]
3. Ren, P.; Pei, P.; Li, Y.; Wu, Z.; Chen, D.; Huang, S.; Jia, X. Diagnosis of water failures in proton exchange membrane fuel cell with zero-phase ohmic resistance and fixed-low-frequency impedance. *Appl. Energy* **2019**, *239*, 785–792. [CrossRef]
4. Dotelli, G.; Ferrero, R.; Stampino, P.G.; Latorrata, S.; Toscani, S. PEM Fuel Cell Drying and Flooding Diagnosis with Signals Injected by a Power Converter. *IEEE Trans. Instrum. Meas.* **2015**, *64*, 2064–2071. [CrossRef]
5. Le Canut, J.-M.; Abouatallah, R.M.; Harrington, D.A. Detection of Membrane Drying, Fuel Cell Flooding, and Anode Catalyst Poisoning on PEMFC Stacks by Electrochemical Impedance Spectroscopy. *J. Electrochem. Soc.* **2006**, *153*, A857. [CrossRef]
6. Yuan, H.; Dai, H.; Wei, X.; Ming, P. Model-based observers for internal states estimation and control of proton exchange membrane fuel cell system: A review. *J. Power Sources* **2020**, *468*, 228376. [CrossRef]
7. Wang, J.; Yang, F.; Ouyang, M. Dieseline fueled flexible fuel compression ignition engine control based on in-cylinder pressure sensor. *Appl. Energy* **2015**, *159*, 87–96. [CrossRef]
8. Zheng, Z.; Petrone, R.; Péra, M.C.; Hissel, D.; Becherif, M.; Pianese, C.; Steiner, N.Y.; Sorrentino, M. A review on non-model based diagnosis methodologies for PEM fuel cell stacks and systems. *Int. J. Hydrogen Energy* **2013**, *38*, 8914–8926. [CrossRef]
9. Arcak, M.; Gorgun, H.; Pedersen, L.M.; Varigonda, S. A nonlinear observer design for fuel cell hydrogen estimation. *IEEE Trans. Control Syst. Technol.* **2004**, *12*, 101–110. [CrossRef]
10. Hu, J.; Xu, L.; Li, J.; Fang, C.; Cheng, S.; Ouyang, M.; Hong, P. Model-based estimation of liquid saturation in cathode gas diffusion layer and current density difference under proton exchange membrane fuel cell flooding. *Int. J. Hydrogen Energy* **2015**, *40*, 14187–14201. [CrossRef]
11. Luna, J.; Husar, A.; Serra, M. Nonlinear distributed parameter observer design for fuel cell systems. *Int. J. Hydrogen Energy* **2015**, *40*, 11322–11332. [CrossRef]
12. Sankar, K.; Jana, A.K. Nonlinear multivariable sliding mode control of a reversible PEM fuel cell integrated system. *Energy Convers. Manag.* **2018**, *1*, 41–565. [CrossRef]
13. Xu, L.; Hu, J.; Cheng, S.; Fang, C.; Li, J.; Ouyang, M.; Lehnert, W. Nonlinear observation of internal states of fuel cell cathode utilizing a high-order sliding-mode algorithm. *J. Power Sources* **2017**, *356*, 56–71. [CrossRef]
14. Yan, C.; Chen, J.; Liu, H.; Lu, H. Model-Based Fault Tolerant Control for the Thermal Management of PEMFC Systems. *IEEE Trans. Ind. Electron.* **2020**, *67*, 2875–2884. [CrossRef]

15. El Aoumari, A.; Ouadi, H.; El-Bakkouri, J.; Giri, F. Adaptive filtered high-gain observer for PEMFC systems in electric vehicles. *Renew. Energy* **2024**, *231*, 120996. [CrossRef]
16. Napoli, G.; Ferraro, M.; Sergi, F.; Brunaccini, G.; Antonucci, V. Data driven models for a PEM fuel cell stack performance prediction. *Int. J. Hydrogen Energy* **2013**, *38*, 11628–11638. [CrossRef]
17. Sun, K.; Esnaola, I.; Okorie, O.; Charnley, F.; Moreno, M.; Tiwari, A. Data-driven modeling and monitoring of fuel cell performance. *Int. J. Hydrogen Energy* **2021**, *46*, 33206–33217. [CrossRef]
18. Li, Z.; Outbib, R.; Hissel, D.; Giurgea, S. Data-driven diagnosis of PEM fuel cell: A comparative study. *Control Eng. Pract.* **2014**, *28*, 1–12. [CrossRef]
19. Çelikdemir, M.Y.; Çelikdemir, S.; Özdemir, M.T. Data driven hybrid feature selection and GPR based modeling for identifying critical fault variables in PEMFCs. *Int. J. Hydrogen Energ.* **2026**, *206*, 153446. [CrossRef]
20. Wang, Y.L.; Wang, Y.F.; Zhao, J.; Xu, J. Observer-based adaptive neural network control for PEMFC air-feed subsystem. *Appl. Soft Comput.* **2021**, *113*, 108003. [CrossRef]
21. Hu, Y.; Zhang, C.; Gong, X.; Gao, J.; Zhang, L.; Chen, H. Design of a nonlinear dynamic output feedback controller based on a fixed-time RBF disturbance observer for a PEMFC air supply system. *Measurement* **2023**, *211*, 112683. [CrossRef]
22. Gu, X.; Hou, Z.; Cai, J. Data-based flooding fault diagnosis of proton exchange membrane fuel cell systems using LSTM networks. *Energy AI* **2021**, *4*, 100056. [CrossRef]
23. Zhao, J.; Li, X.; Shum, C.; McPhee, J. A Review of physics-based and data-driven models for real-time control of polymer electrolyte membrane fuel cells. *Energy AI* **2021**, *6*, 100114. [CrossRef]
24. Hickner, M.A.; Siegel, N.P.; Chen, K.S.; Hussey, D.S.; Jacobson, D.L.; Arif, M. In Situ High-Resolution Neutron Radiography of Cross-Sectional Liquid Water Profiles in Proton Exchange Membrane Fuel Cells. *J. Electrochem. Soc.* **2008**, *155*, B427–B434. [CrossRef]
25. Sasabe, T.; Tsushima, S.; Hirai, S. In-situ visualization of liquid water in an operating PEMFC by soft X-ray radiography. *Int. J. Hydrogen Energy* **2010**, *35*, 11119–11128. [CrossRef]
26. Bedet, J.; Maranzana, G.; Leclerc, S.; Lottin, O.; Moyne, C.; Stemmelen, D.; Mutzenhardt, P.; Canet, D. Magnetic resonance imaging of water distribution and production in a 6 cm^2 PEMFC under operation. *Int. J. Hydrogen Energy* **2008**, *33*, 3146–3149. [CrossRef]
27. Lin, R.; Yu, H.; Zhong, D.; Han, L.; Lu, Y.; Tang, S.; Hao, Z. Investigation of real-time changes and recovery of proton exchange membrane fuel cell in voltage reversal. *Energy Convers. Manag.* **2021**, *236*, 114037. [CrossRef]
28. Ma, Y.; Lin, R.; Hou, Z.; Wang, R.; Wang, Y.; Ji, W. Research on the variation of current density distribution in a commercial-size proton exchange membrane fuel cell under dynamic gas operation parameters. *Int. J. Heat Mass Transf.* **2022**, *196*, 123287. [CrossRef]
29. Tang, Z.; Huang, Q.-A.; Wang, Y.-J.; Zhang, F.; Li, W.; Li, A.; Zhang, L.; Zhang, J. Recent progress in the use of electrochemical impedance spectroscopy for the measurement, monitoring, diagnosis and optimization of proton exchange membrane fuel cell performance. *J. Power Sources* **2020**, *468*, 228361. [CrossRef]
30. Yuan, H.; Dai, H.; Ming, P.; Zhao, L.; Tang, W.; Wei, X. Understanding dynamic behavior of proton exchange membrane fuel cell in the view of internal dynamics based on impedance. *Chem. Eng. J.* **2022**, *431*, 134035. [CrossRef]
31. Rezaei Niya, S.M.; Hoorfar, M. Study of proton exchange membrane fuel cells using electrochemical impedance spectroscopy technique—A review. *J. Power Sources* **2013**, *240*, 281–293. [CrossRef]
32. Zhang, S.Z.; Dai, H.F.; Yuan, H.; Ming, P.; Wei, X. Sensibility Study on Electrochemical Impedance of Proton Exchange Membrane Fuel Cell. *J. Mech. Eng.* **2021**, *57*, 40. [CrossRef]
33. Dotelli, G.; Ferrero, R.; Stampino, P.G.; Latorrata, S.; Toscani, S. Diagnosis of PEM Fuel Cell Drying and Flooding Based on Power Converter Ripple. *IEEE Trans. Instrum. Meas.* **2014**, *63*, 2341–2348. [CrossRef]
34. Kadyk, T.; Hanke-Rauschenbach, R.; Sundmacher, K. Nonlinear frequency response analysis of PEM fuel cells for diagnosis of dehydration, flooding and CO-poisoning. *J. Electroanal. Chem.* **2009**, *630*, 19–27. [CrossRef]
35. Touhami, S.; Dubau, L.; Mainka, J.; Dillet, J.; Chatenet, M.; Lottin, O. Anode aging in polymer electrolyte membrane fuel Cells I: Anode monitoring by ElectroChemical impedance spectroscopy. *J. Power Sources* **2021**, *481*, 228908. [CrossRef]
36. Moçotéguy, P.; Ludwig, B.; Beretta, D.; Pedersen, T. Study of the impact of water management on the performance of PEMFC commercial stacks by impedance spectroscopy. *Int. J. Hydrogen Energy* **2020**, *45*, 16724–16737. [CrossRef]
37. Brunetto, C.; Moschetto, A.; Tina, G. PEM fuel cell testing by electrochemical impedance spectroscopy. *Electr. Power Syst. Res.* **2009**, *79*, 17–26. [CrossRef]
38. Katayama, N.; Kogoshi, S. Real-Time Electrochemical Impedance Diagnosis for Fuel Cells Using a DC–DC Converter. *IEEE Trans. Energy Convers.* **2015**, *30*, 707–713. [CrossRef]
39. Debenjak, A.; Boškoski, P.; Musizza, B.; Petrovcic, J.; Juricic, D. Fast measurement of proton exchange membrane fuel cell impedance based on pseudo-random binary sequence perturbation signals and continuous wavelet transform. *J. Power Sources* **2014**, *254*, 112–118. [CrossRef]

40. Manganiello, P.; Petrone, G.; Giannattasio, M.; Monmasson, E.; Spagnuolo, G. FPGA implementation of the EIS technique for the on-line diagnosis of fuel-cell systems. In Proceedings of the 2017 IEEE 26th International Symposium on Industrial Electronics (ISIE), Edinburgh, UK, 19–21 June 2017; pp. 981–986. [CrossRef]
41. Lu, H.; Chen, J.; Yan, C.; Liu, H. On-line fault diagnosis for proton exchange membrane fuel cells based on a fast electrochemical impedance spectroscopy measurement. *J. Power Sources* **2019**, *430*, 233–243. [CrossRef]
42. Kurz, T.; Hakenjos, A.; Krämer, J.; Zedda, M.; Agert, C. An impedance-based predictive control strategy for the state-of-health of PEM fuel cell stacks. *J. Power Sources* **2008**, *180*, 742–747. [CrossRef]
43. Dotelli, G.; Ferrero, R.; Stampino, P.G.; Latorrata, S. Analysis and Compensation of PEM Fuel Cell Instabilities in Low-Frequency EIS Measurements. *IEEE Trans. Instrum. Meas.* **2014**, *63*, 1693–1700. [CrossRef]
44. Kitamura, N.; Manabe, K.; Nonobe, Y.; Kizaki, M. *Development of Water Content Control System for Fuel Cell Hybrid Vehicles Based on AC Impedance*; SAE 2010 World Congress & Exhibition; SAE International: Warrendale, PA, USA, 2010. [CrossRef]
45. Reilly, T. Sensitivity Analysis for Dependent Variables. *Decis. Sci.* **2000**, *31*, 551–572. [CrossRef]
46. Fouquet, N.; Doulet, C.; Nouillant, C.; Dauphin-Tanguy, G.; Ould-Bouamama, B. Model based PEM fuel cell state-of-health monitoring via ac impedance measurements. *J. Power Sources* **2006**, *159*, 905–913. [CrossRef]
47. Chen, H.; Zhao, X.; Zhang, T.; Pei, P. The reactant starvation of the proton exchange membrane fuel cells for vehicular applications: A review. *Energy Convers. Manag.* **2019**, *182*, 282–298. [CrossRef]
48. Ma, T.; Lin, W.; Zhang, Z.; Kang, J.; Yang, Y. Research on electrochemical impedance spectroscope behavior of fuel cell stack under different reactant relative humidity. *Int. J. Hydrogen Energy* **2021**, *46*, 17388–17396. [CrossRef]
49. Yan, X.; Hou, M.; Sun, L.; Liang, D.; Shen, Q.; Xu, H.; Ming, P.; Yi, B. AC impedance characteristics of a 2 kW PEM fuel cell stack under different operating conditions and load changes. *Int. J. Hydrogen Energy* **2007**, *32*, 4358–4364. [CrossRef]
50. Christopher Frey, H.; Patil, S.R. Identification and Review of Sensitivity Analysis Methods. *Risk Anal.* **2002**, *22*, 553–578. [CrossRef]
51. Benesty, J.; Chen, J.; Huang, Y. On the Importance of the Pearson Correlation Coefficient in Noise Reduction. *IEEE Trans. Audio Speech Lang. Process.* **2008**, *16*, 757–765. [CrossRef]
52. Jiang, P.; Chen, J.; Jin, L.; Kumar, L. Adaptive Condition Monitoring for Fuel Cells Based on Fast EIS and Two-Frequency Impedance Measurements. *IEEE Trans. Ind. Electron.* **2023**, *70*, 8517–8525. [CrossRef]
53. Wang, Y.; Zhang, H.; Liu, K.; Hu, M.; Wu, Z.; Zhang, C.; Hua, W. A Forward Compensation Method to Eliminate DC Phase Error in SRF-PLL. *IEEE Trans. Power Electron.* **2022**, *37*, 6280–6284. [CrossRef]
54. Xin, Z.; Wang, X.; Qin, Z.; Lu, M.; Loh, P.C.; Blaabjerg, F. An Improved Second-Order Generalized Integrator Based Quadrature Signal Generator. *IEEE Trans. Power Electron.* **2016**, *31*, 8068–8073. [CrossRef]
55. Ge, X.K.; Li, W.; Tian, W.; Wang, R.; Wan, X.; Tang, H. Efficiency improvement strategy of fuel cell system based on oxygen excess ratio and cathode pressure two-dimensional optimization. *Int. J. Hydrogen Energy* **2024**, *57*, 136–147. [CrossRef]